Pressure Measurements Using an Airborne Differential Absorption Lidar. Part I: Analysis of the Systematic Error Sources

CYRILLE N. FLAMANT*

University of Maryland at College Park, College Park, Maryland

GEARY K. SCHWEMMER AND C. LAURENCE KORB

Laboratory for Atmospheres, NASA/Goddard Space Flight Center, Greenbelt, Maryland

KEITH D. EVANS

Joint Center for Earth Systems Technology, University of Maryland Baltimore County, Catonsville, Maryland

STEPHEN P. PALM

Science Systems and Applications Inc., Seabrook, Maryland

(Manuscript received 15 July 1997, in final form 24 July 1998)

ABSTRACT

Systematic error sources that require correction when making remote airborne measurements of the atmospheric pressure field in the lower troposphere, using an oxygen differential absorption lidar, are analyzed. A detailed analysis of this measurement technique is provided, which includes corrections for imprecise knowledge of the detector background level, the oxygen absorption line parameters, and variations in the laser output energy. In addition, the authors analyze other possible sources of systematic errors, including spectral effects related to aerosol and molecular scattering, water vapor vertical distribution, interference by rotational Raman scattering, and interference by isotopic oxygen lines.

1. Introduction

Measurement of the atmospheric pressure field is desirable for improving weather forecasting in the midlatitudes since the location of high and low pressure areas determine the weather patterns. Furthermore, the storm regime and fronts are important weather phenomena and produce significant air–sea interaction and planetary boundary layer (PBL) fluxes (Brown and Levy 1986). The frontal location and mesoscale dynamics of midlatitude storm systems are difficult to define with conventional analysis, partly because of mesoscale variability in both the atmosphere and ocean, which is generally observed to be very large. Bond and Feagle (1985) suggested that atmospheric dynamics take place on scales that are not practically resolvable with conventional methods.

Better determination of the winds, stress, sea surface temperature, and frontal location is essential for progress in these mesoscale modeling efforts. Nuss and Brown (1987) have shown that the primary limitation on the accuracy of the models was the sparsity of the input data. Remote sensing instruments are likely candidates to supplement the existing observational network with additional data at a density usable for routine synoptic-scale analyses.

Differential absorption lidar (DIAL) provides the only direct remote measurement of atmospheric pressure with high spatial resolution and precision. The theory of using the DIAL technique to measure atmospheric pressure has been described by Korb and Weng (1983). The lidar system used in these measurements has been described by Schwemmer et al. (1987), and earlier measurements from ground and aircraft reported have been by Korb et al. (1989) and Starr et al. (1992). We describe here the detailed analysis of the various potential systematic error sources of DIAL pressure measurements. In a companion paper (hereafter referred to as Part II)

* Current affiliation: Service d'Aéronomie du CNRS, Université Pierre et Marie Curie, Paris, France.

Corresponding author address: Geary K. Schwemmer, NASA/Goddard Space Flight Center, Code 912, Greenbelt, MD 20771.
E-mail: geary@virl.gsfc.nasa.gov

we describe the development and application of the correction techniques as applied to a series of measurements made from an aircraft off the east coast of the United States during June and July of 1989.

High spectral resolution DIAL (defined as requiring a laser bandwidth of less than 0.05 cm^{-1}) is a particularly complicated technique, both from an instrumental perspective and from an analysis perspective. The pressure measurement is more forgiving than DIAL measurements of temperature and specific humidity that operate with a laser centered on narrow absorption lines. This is because the pressure measurement is made in the much broader, flatter absorption trough between lines. There are still, however, many opportunities for systematic errors to enter the data. Thus, we have attempted to evaluate as many sources of error as possible within this study before applying corrections to the data collected from the flight experiments.

The instrument typically must include one or more tunable high spectral resolution lasers, preferably single frequency with very high spectral purity, that is, very low broadband emission or out-of-band frequencies. One laser, the online laser, is tuned to the oxygen spectral absorption feature of interest, while the second, the offline laser, is tuned to a nearby unabsorbed frequency. The lasers are fired nearly simultaneously, and the resulting two return signals must be accurately superimposed in order to be able to ratio them to determine the atmospheric transmission as a function of range or altitude. Since the data are digitally sampled at discrete time intervals, the time (or range) of any given sample in one laser return must accurately correspond to the time (or range) of the corresponding sample in the other laser return signal. Backscatter by molecules is double Doppler broadened, and has a width approximately equal to twice the Doppler width of the absorption lines. On the other hand, the backscatter from aerosols is very narrow and is nearly identical to the outgoing laser emission. (Doppler broadening caused by the motion of aerosols is negligible compared to the width of the oxygen absorption lines.) Effects due to this complexity have been discussed by Theopold and Bosenberg (1993) for temperature measurements, and by Ansmann (1985) as well as Ansmann and Bosenberg (1987) with respect to water vapor measurements. Accordingly, a measurement of the aerosol to molecular backscatter ratio must be derived from the offline (or reference) return signal. In addition, oxygen and nitrogen rotational Raman scattering contribute a signal, which is over 3% of the molecular backscatter, if not filtered out, as is the case with the measurements discussed in Part II. Since rotational Raman backscatter is spectrally spread out over tens of wavenumbers from the laser frequency, it is only weakly absorbed on the return path to the lidar receiver and can dominate the online return signal from large distances. These and other systematic effects are carefully evaluated in the following analysis.

TABLE 1. Lidar system and data acquisition characteristics.

Transmitter	
Beam divergence	2.5 mrad
Offline output energy (measured)	38 mJ
Offline laser wavelength	757.49 nm
Online laser wavelength	760.32 nm
Receiver	
Telescope aperture	0.1115 m^2
Optical throughput	0.55
Detector quantum efficiency	7% at 760 nm
Transimpedance amplifier gain	3000 V A^{-1}
Photomultiplier gain	2×10^4
Data system	
Altimeter clock sample rate (range bin)	80 MHz (1.875 m)
Data acquisition sample rate (range bin)	5 MHz (30 m)
Red pass filter cutoff wavelength	720 nm

In section 2 we briefly describe the lidar system. Section 3 provides an overview of the DIAL pressure measurement theory and practical implementation. Section 4 reviews the possible instrumental errors sources. In section 5, the systematic errors on the pressure measurements caused by atmospheric effects are quantified. A detailed description is given of how one can correct for these effects. In the last section we summarize and give conclusions.

2. System description

Nighttime measurements were made with a dual-alexandrite laser–lidar system mounted in a nadir-pointing position in the National Aeronautic and Space Administration (NASA) Electra aircraft over the Atlantic Ocean off the east coast of the United States. Key system and data acquisition parameters are summarized in Table 1. Pressure was derived from measurements of the atmospheric transmission in the trough region between the RR13 and RQ14 lines of the oxygen A band, at a vacuum wavenumber of 13 152.38 cm^{-1}, or 760.32-nm wavelength in surface pressure air. The offline or reference laser wavelength was 757.49 nm. The online laser was fired first rephasing the digitizer clock and after a few microseconds delay, 500 digitized samples of the return signal were recorded. Three hundred μs later the offline laser was fired, the digitizer clock was again rephased, and another 500 samples containing the offline return signal were stored. A few milliseconds before the next pulse pair, the data acquisition system was triggered to make a background measurement that was subtracted from the set of laser return signals that followed. The entire sequence was repeated every 100 ms, and all data were recorded. Except where stated otherwise, 100 shots are averaged prior to signal processing.

A second photomultiplier (PMT) was used as an altimeter. By counting the number of clock pulses from the time the laser fired to the time the surface reflection arrived at this PMT, we measured the aircraft altitude to a resolution of 1.9 m. The altimeter was calibrated

by ranging to a hard target, while the aircraft was situated on the ground, and by comparing the result to a second, calibrated laser ranger. Having the altimeter measurement made simultaneously with the pressure measurement is important for establishing an absolute calibration to the altitude of the pressure measurements.

In addition to the lidar system, a Navigation and Environmental Measurements System (NEMS) collected data from a Loran navigation instrument, aircraft pitch and roll from gyroscopes, cabin pressure, outside air temperature, dewpoint, and static pressure. Radiosondes were launched from Wallops Island at the beginning of each flight and hourly thereafter. The balloons were tracked by radar to determine their geometric altitude and the wind vector as they ascended.

3. Theory of pressure measurements and calibration procedure

The return signal intensity for both the online and offline signals are range-squared corrected as well as laser energy corrected. The latter correction is done using energy monitor values made with a photoconductive silicon photodiode and a charge-integrating digitizer that integrates over the 100-ns laser pulses. Although the energy monitor corrections were found to have some systematic errors that needed to be calibrated out as described in this section, it is still useful to apply a shot-by-shot correction, which helps to reduce signal variance due to instability in the laser pulse energy. This variance tended to be on the order of 5% root-mean-square in our lasers. Corrections are made according to

$$S_i(z) = \frac{1}{N}\sum_{j=1}^{N}\left[\frac{S_{ij}(z)}{E_{ij}}\right] \times \overline{E_i}$$

where

$$\overline{E_i} = \frac{1}{N}\sum_{j=1}^{N} E_{ij}, \tag{1}$$

where i can be read as online or offline, j is the shot number, N is number of shots, E is the energy monitor value, and S is the lidar signal value.

The optical power received goes through the detection chain, and the output signal S, in counts, is related to the optical power P by

$$S(z) = \frac{P(z)}{h\nu c} G e^{-} R_e D, \tag{2}$$

where h is Planck's constant, ν is the laser offline or online wavenumber, G is the gain of the PMT dynode chain, e^{-} is the charge of an electron, D is the volts-to-counts (analog to digital) conversion factor, c is the speed of light, and R_e is the equivalent resistance of the transimpedence amplifier.

Since both online and offline signals are measured with a single detector and both energy monitor signals are made with a single detector, then in calculating the transmission, all constants should factor out and the transmission profile $\tau(z)$ is given as

$$\tau(z) = \left[\frac{P_{\text{on}}(z)}{P_{\text{off}}(z)}\right]\left(\frac{E_{\text{off}}}{E_{\text{on}}}\right), \tag{3}$$

where P_{on} and P_{off} are the detected optical power for the online and offline channel (ignoring any molecular broadening), respectively, given by

$$P_{\text{on}}(z) = \frac{AT_0}{(z_{\text{ref}} - z)^2}\eta E_{\text{on}}\frac{c}{2}[\beta_{p,\text{on}}(z) + \beta_{m,\text{on}}(z)] \times \exp\left\{-2\int_{z_{\text{ref}}}^{z}[K(r) + \alpha_{p,\text{on}}(r) + \alpha_{m,\text{on}}(r)]\,dr\right\} \tag{4a}$$

and

$$P_{\text{off}}(z) = \frac{AT_0}{(z_{\text{ref}} - z)^2}\eta E_{\text{off}}\frac{c}{2}[\beta_{p,\text{off}}(z) + \beta_{m,\text{off}}(z)] \times \exp\left\{-2\int_{z_{\text{ref}}}^{z}[\alpha_{p,\text{off}}(r) + \alpha_{m,\text{off}}(r)]\,dr\right\}, \tag{4b}$$

where η is the detector quantum efficiency at 760 nm, T_0 is the receiver optical throughput (or one-way transmission), A is the surface area of the telescope, E_{on} and E_{off} are the online and offline laser output energies, α_p and α_m are the aerosol (particulate) and Rayleigh (molecular) extinction coefficients, β_p and β_m are the aerosol and Rayleigh backscatter coefficients, K is the oxygen resonant absorption coefficient that is essentially zero at the offline frequency we selected for the pressure measurements, z is the altitude, and z_{ref} is the aircraft altitude. Our online and offline wavelengths are separated by 3 nm. Using the manufacturer's nominal curves, we calculated a change in η from the online to the offline wavelength of about 1 part in 1000, which is small compared to our other corrections and is equivalent to an error in the energy monitor ratio, which is explicitly corrected for. Similarly, any errors in T_0 will be implicitly corrected for with the energy monitor correction. The normal DIAL simplifying assumption of ignoring any wavelength dependence of all variables except K is made for the moment to effect a solution for pressure. The wavelength dependence of the extinction and backscatter coefficients will be treated in the sections on atmospheric effects. Introducing Eqs. (4a) and (4b) in Eq. (3), and accounting for the pitch and roll angles as they increase the path over which the absorption coefficient is calculated, we find

$$\tau(z) = \exp\left[-\frac{2}{\cos\theta_p\,\cos\theta_r}\int_{z_{\text{ref}}}^{z} K(r)\,dr\right]. \tag{5}$$

The measured transmission for each altitude is com-

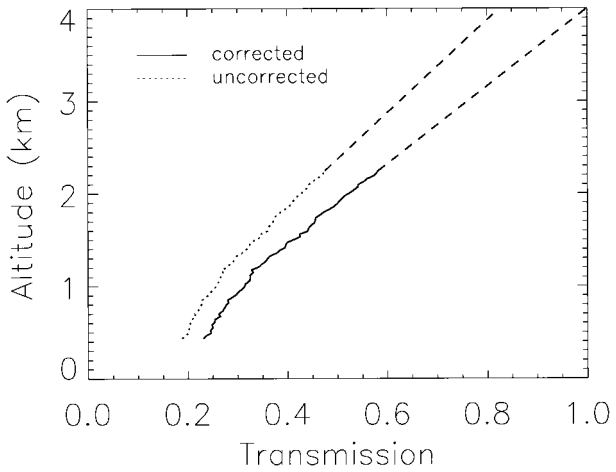

FIG. 1. Oxygen transmission profile before (dotted line) and after (solid line) calibration using a pressure sounding. Note that only the corrected transmission profile goes through unity at the height of the aircraft (4 km in this case). This is illustrated by the dashed line, representing the extrapolated profiles up to the aircraft altitude.

puted from the lidar return signals using Eq. (3) in the region between the gating turn-on transient and the surface return. Korb and Weng (1983) state that the one-way oxygen absorption optical depth is

$$\int_{z_{\text{ref}}}^{z} K(r)\, dr = C|p^2(z) - p^2(z_{\text{ref}})|, \tag{6}$$

where $p(z)$ and $p(z_{\text{ref}})$ are the pressure at altitudes z and z_{ref}, and C is an experimentally determined calibration constant. Higher-order terms can be neglected for the limited range of altitudes encountered in our experimental measurements. Solving for $p(z)$,

$$p(z) = \left[-\frac{\cos\theta_p \cos\theta_r}{2}\frac{\ln\tau(z_{\text{ref}}, z)}{C} + p^2(z_{\text{ref}})\right]^{1/2}. \tag{7}$$

The term $p(z_{\text{ref}})$ is acquired with the NEMS on the aircraft and z_{ref} is measured with the altimeter channel of the lidar system. Also, $\tau(z_{\text{ref}}, z)$ is the lidar-measured atmospheric transmission with a correction applied for systematic errors in the measurement of the ratio of the laser energies. Next we describe the method used to find the calibration constant C and the laser energy ratio correction to the measured transmission.

It was observed that the transmission calculated from Eq. (3) and extrapolated back to the altitude of the aircraft was not unity (Fig. 1). We attribute this to an error in the measurement of the relative energy in each laser pulse based on a laboratory assessment using two similar photodiode detectors. A systematic correction was developed, as part of the absolute calibration, based on the lidar data and balloon sounding in order to force the transmission to one at the aircraft altitude. Let us consider two regions of the atmosphere sampled by the lidar: the near field and the far field, which correspond to atmospheric layers relatively close to the aircraft and the surface, respectively. Their depth is chosen such that the signal-to-noise ratio is greater than 5 in the layers. Let $\tau_m(z_{\text{ref}}, z)$ be the lidar-measured transmission between the aircraft and altitude z. If both the transmission measured in the far and near fields are in error by the same factor, then we can determine the correct transmission for the atmospheric path between the near and far fields by the ratio of the two measured transmissions:

$$\frac{\tau_m(z_{\text{ref}}, z_{\text{far}})}{\tau_m(z_{\text{ref}}, z_{\text{near}})} = \exp\left[-\frac{2}{\cos\theta_p \cos\theta_r}\int_{z_{\text{near}}}^{z_{\text{far}}} K(r)\, dr\right]. \tag{8}$$

Using Eq. (8) in Eq. (6) we solve for the calibration constant C:

$$C = -\frac{\cos\theta_p \cos\theta_r}{2}\ln\frac{\tau_m(z_{\text{ref}}, z_{\text{far}})}{\tau_m(z_{\text{ref}}, z_{\text{near}})}\Bigg/|p^2(z_{\text{far}}) - p^2(z_{\text{near}})|. \tag{9}$$

Radar tracking of the target trailing the meteorological package provides us with the exact balloon altitude at all times. A parabola is fit to these independent measurements of pressure (from radiosonde) and altitude (from radar) for the first 3000 m. The parabola is then used to interpolate between radiosonde data points to get the pressure at z_{far} and z_{near}. To minimize the calibration error due to noise in the measurements, values of the lidar-measured transmissions are averaged over 180 m in altitude in the near and far fields. We calculate the value of C for the transmission profile taken nearest in time and space to a radiosonde profile on the order of 1.5×10^{-6} hPa^{-2}.

The errors associated with the accurate knowledge of $p(z_{\text{far}})$ and $p(z_{\text{near}})$ can be estimated by artificially shifting the radar altitude with respect to the radiosonde data. A $\pm$4-hPa uncertainty of the pressure measurements leads to a $\pm$1.5% error on the calibration constant C. Accounting for this error and an uncertainty of 10% on the pressure measurements made on board the aircraft (which is unrealistically large since the precision on the instrument is less than 1 hPa), the overall error on pressure calculated with Eq. (7) is less than 1% throughout the lower troposphere.

To correct the measured transmission for the energy monitor error, we first calculate the corrected transmission profile in the near field $\tau_c(z_{\text{near}})$, using Eqs. (5), (6), and (9):

$$\tau_c(z_{\text{ref}}, z_{\text{near}}) = \exp\left[-\frac{2C}{\cos\theta_p \cos\theta_r}|p^2(z_{\text{near}}) - p^2(z_{\text{ref}})|\right]. \tag{10}$$

The correction factor $\tau_c(z_{\text{ref}}, z_{\text{near}})/\tau_m(z_{\text{ref}}, z_{\text{near}})$ is then applied to the entire transmission profile. The corrected vertical transmission profile is given by

$$\tau(z_{\text{ref}}, z) = \left[\tau_m(z_{\text{ref}}, z)\frac{\tau_c(z_{\text{ref}}, z_{\text{near}})}{\tau_m(z_{\text{ref}}, z_{\text{near}})}\right]. \tag{11}$$

Figure 1 shows an uncorrected and a corrected transmission profile made from measured lidar signals.

4. Instrumental error sources

Baseline errors in the lidar signals will contribute to systematic errors in the derivation of pressure with the same sensitivity as random errors in the signals, only with much more devastating effects since no amount of averaging can remove them. We refer the reader to Korb and Weng (1983) for a discussion of the sensitivity of the pressure measurement to errors in the lidar return signals and only give a brief discussion of the systematic error sources related to the instrumentation.

a. Ambient light background and lidar signal baseline subtraction

Five milliseconds prior to firing the laser, the data system acquires the background of ambient atmospheric light scattered in the direction of the telescope. The background signal is then subtracted from the subsequent lidar return signals in real time and the signal minus background was recorded on tape. The gain of the PMT changes during the transient, however, so we routinely exclude at least the first microsecond of data from analysis. An error in the measurement and subtraction of the background signal will have the same effect as an error in the lidar signal baseline discussed next.

PMTs typically exhibit an elevated dark current for some time after exposure to a bright light source, even to some extent if the PMT was off when exposed. Lidar return signal data are recorded between the altitude of the aircraft to the equivalent of 11 km below the surface. In previous work by Korb et al. (1989) and Starr et al. (1992), the return signal below the surface was used to define a baseline reference for each shot to correct for this signal-induced bias. Strong backscatter signals are usually received from the near-field backscatter, from clouds, and the surface return. Near-field blinding of the PMT is eliminated by setting to zero the voltage between the photocathode and the first dynode for a few microseconds. Then the digitization gates were open 100 μs, which was long enough for the saturated signal to decay to a suitable baseline value. Previously, Korb et al. (1989) would average 100 values along the tail end of the signal, then subtract from the near-field return a value equal to this tail value and assume it is constant throughout the signal, which is not strictly true. An improved PMT (Hamamatsu R1017) was used for the data discussed here and was tested in the laboratory prior to its use in the field. Lee et al. (1989) have measured the response function of this PMT, which after the first 10 μs, decays exponentially with a 7-μs time constant. They found that an unsaturated pulse peak should have a negligible baseline value (close to zero). Therefore, we applied no such extra baseline subtraction to the data discussed here. Verification of the background subtraction and baseline assumption was made by introducing a baseline shift to our measured signals and reprocessing the data to retrieve 125 pressure profiles along one flight track. The mean of the differences between the radiosonde and the lidar pressures and the variance at each altitude in the lidar data are a minimum without any baseline shift. Shifts of ± 10 counts ($\approx 2\%$ of the median signal level) induce an average 3-hPa bias, unevenly distributed with altitude and peaking at about 6 hPa at an altitude of 1500 m. It also increases the standard deviation along the flight track from 4.0 to 4.3 hPa. The standard deviations were taken at each altitude using the 125 pressure profiles along the flight track, not from the 100 signal average used to make each pressure retrieval, so they include atmospheric variance. The individual pressure retrievals had root-mean-square differences from the sonde pressure profiles of 1–2 hPa.

b. Laser-blocked data and offline/offline lidar data

To test for possible ground loops in the signals, we looked at in-flight-acquired data in which the laser beams were blocked from exiting the aircraft. We also took data with both lasers tuned to the same offline frequency, which we call off–off data, to check the signal altitude registration and the background subtraction.

For blocked data measurements, the regular background and return signal recording sequence takes place without the laser beam going out to the atmosphere so that the signal detected for both acquisitions should be proportional to the atmospheric background. In the case where no ground loop exists and without the background subtraction, the ratio of the online to the offline should be equal to unity and not vary with range but should be noisy because of the small quantities being ratioed. In the case of a ground loop; the strong flash lamp current pulse (≥ 100 A) will perturb the potential of the local ground, which manifests itself as a signal in single-ended inputs if there is a ground current path for this pulse through the detection system. The receiver will register an output signal added to the background, and the ratio of the online to offline signal will not be unity or constant with range. Ground loops are eliminated by careful design of the electronics and data acquisition system and thorough testing, ensuring there is only a single ground path from the detector to earth ground and that no part of it includes laser electronics. This was tested with an ohmmeter and a floating oscilloscope set to a gain of 100 μV per division. Other than the small transient due to the switching of the gate voltage, there was no evidence of a ground loop on the receiver signals at the 10-μV limiting resolution, which corresponds to 0.04 counts. Nor was ground loop interference found to affect the recorded data. Ground loop errors would show up as a slope or low-frequency swing to laser-blocked data (Fig. 2). Ground loop currents are

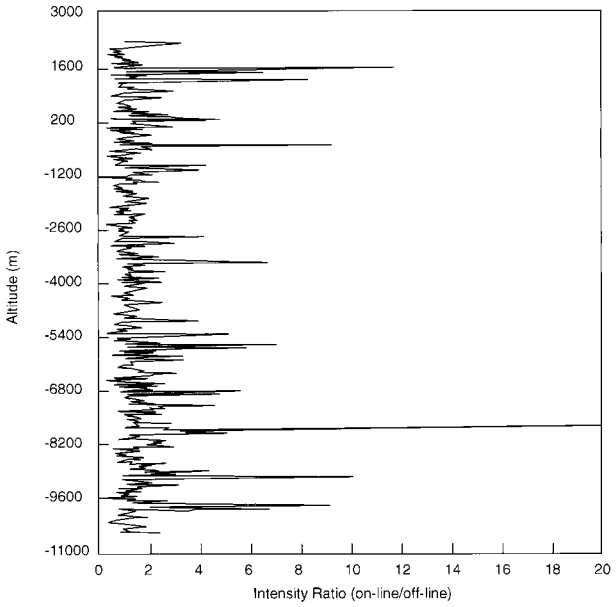

FIG. 2. Ratio of 100 shot averages of the online to the offline signal in the case where the laser beam is prevented from going out to the atmosphere. In the event that no ground loop affects the data, the signal detected for both acquisitions should be proportional to the atmospheric background, and the ratio of the online to the offline should be equal to unity and constant with range. Noise in the data results from the small quantities being ratioed.

typically induced by laser flashlamp currents or line (60 Hz) currents.

Off–off measurements are made in flight by tuning both lasers to the same wavelength, which correspond in this case to the offline wavelength. If the lasers sample the same atmospheric layer at the same time, the return signal on both channels should be proportional and their ratio should be constant with altitude. If one channel starts recording before the other, aerosol features will not be registered at the same altitude and large oscillations in the ratio of the two signals will be generated. Except for some near-field discrepancies, which are due to slightly different divergence characteristics of the two lasers, the signal ratio yields a constant with altitude. Note that a relatively large (8 mrad) telescope field of view creates an overlap function that quickly converges to unity, at about 50 m distance.

c. Aircraft pitch, roll, and altitude corrections

The nadir direction for the outgoing laser beam is calculated so as to account for the nominal in-flight aircraft pitch angle of $+2°$ (nose up). On the ground, the airplane pitch angle is $-2°$, so the laser beam is aligned toward the back of the aircraft at a 4° angle from the vertical when on the ground. In flight, the beam is pointing straight down.

Both pitch and roll are measured using gyros, and the data are recorded on the NEMS acquisition computer. In the postexperiment analysis, we generate 100-shot averaged lidar profiles, add the NEMS data to the records, and use the roll and pitch information to correct the altitudes of the backscattered signals and the optical depths.

The altitude of the aircraft is measured from the signal reflected off the surface and is corrected for the pitch and roll angles and an 18-m calibration offset. Neglecting the aircraft displacement during the laser pulse roundtrip time (3 mm at a 4-km altitude for a speed of 120 m s^{-1}), we assume that the laser beam roundtrip is achieved on the same path. If the surface reflection signal is not above the altimeter discriminator threshold, an erroneous altitude retrieval results. Those shots were filtered out (on the order of 10 shots per flight leg).

5. Atmospheric systematic effects on measured transmission

In this section we consider the effects of rotational Raman scattering, strong aerosol gradients, wavelength dependence of the aerosol backscatter coefficient, Doppler broadening in the presence of an isotopic oxygen line, and water vapor vertical distribution. All these processes require a knowledge of the relative contributions of Rayleigh and Mie scattering to the lidar signals, which can be derived from a lidar equation inversion procedure. For a monostatic, monochromatic, pulsed lidar, the expression of the backscatter coefficient is obtained by solving a Bernoulli-type differential equation (Klett 1985). Solving the lidar equation requires the knowledge of the total (aerosol plus molecular) backscatter to extinction ratio ($\phi = \beta/\alpha$) and of a boundary condition at a reference height z_{ref}. Whenever the boundary condition is taken closest to the source (the lidar), the solution is referred to as unstable (or forward). In the case of airborne nadir lidar measurements, the unstable solution is generally used because measurements of the boundary condition (BC or ''reference'') at the far end of the domain (the surface of the ocean) are difficult to make simultaneously to lidar measurements, whereas an onboard nephelometer, for example, can provide measurements of aerosol optical properties near the aircraft.

For a backscatter-to-extinction ratio variable with altitude, the unstable solution (Klett 1985) is given by

$$\beta_{\text{off}}(z) = \frac{(z_{\text{ref}} - z)^2 S_{\text{off}}(z)}{\dfrac{1}{C^*} - 2\displaystyle\int_{z_{\text{ref}}}^{z} \dfrac{(z_{\text{ref}} - r)^2 S_{\text{off}}(r)\, dr}{\phi(r)}}, \quad (12)$$

where $(z_{\text{ref}} - z)^2 S_{\text{off}}$ is the range-squared corrected, energy-normalized signal and C^* is the backscatter system constant (in m^{-3} per count), given by

$$C^* = \frac{2h\mu}{AT_0\eta E_{\text{off}} G e^- R_e D}. \quad (13)$$

Equation (13) holds only in the vinicity of the laser source. The expression $C^*(z_{\text{ref}} - z)^2 S_{\text{off}}$ is often referred

to as the reference backscatter coefficient needed in order to initiate the lidar equation inversion procedure generally used to infer extinction and/or backscatter coefficient measurements from lidar measurements (Klett 1985).

The backscatter ratio R [$R = (\beta_{p,\text{off}} + \beta_{m,\text{off}})/\beta_{m,\text{off}}$] is retrieved from the offline range-squared corrected lidar signal using Eq. (12). We apply a boundary condition to the level in the atmosphere that presents the smallest signal variance. By examining the range-squared corrected signals, this region was found near 2-km altitude and is discussed in further details in Part II. Flamant et al. (1998) have shown that a reference value of the total backscatter coefficient near the surface could be derived from the lidar signal in the PBL and the intensity of the surface return (provided that it is not saturated), which in turn relates to sea surface reflectance and surface wind speed (Cox and Munk 1954; Bufton et al. 1983).

Flamant et al. (1998), during SOFIA and SEMAPHORE,[1] as well as Flamant and Pelon (1996), during PYREX,[2] have reported a value of the scattering ratio of $R = 1.5$ at an altitude of 2 km above both the Atlantic and the Mediterranean. These values were obtained from extinction measurements made around 0.5 μm by a nephelometer carried on board an aircraft. At a wavelength of 760 nm, the value of this ratio is expected to be larger, although values of $R = 1.2$ have been observed (Sasano and Browell 1989). To estimate the errors on the pressure retrievals caused by rotational Raman scattering, the wavelength dependence of the aerosol backscatter coefficient, and Doppler broadening in the presence of an isotopic oxygen line, the boundary condition of $R = 1.5 \pm 0.3$ at 2 km is taken in the following sections.

The ratio of the offline lidar signal in the PBL to the offline lidar signal in the free troposphere varies between 2 and 3, on average. The backscatter ratio in the PBL will then range from 2.4 to 5.4 if we assume the transmission to be small. In Fig. 3 we show representative backscatter ratio profiles calculated from our data in nearly neutral stratification conditions with R equal to 1.2, 1.5, and 1.8. In slightly unstable conditions, this ratio is expected to be larger.

a. Rotational Raman scattering

The measurements discussed in Part II were taken at night with a broadband optical filter in the receiver,

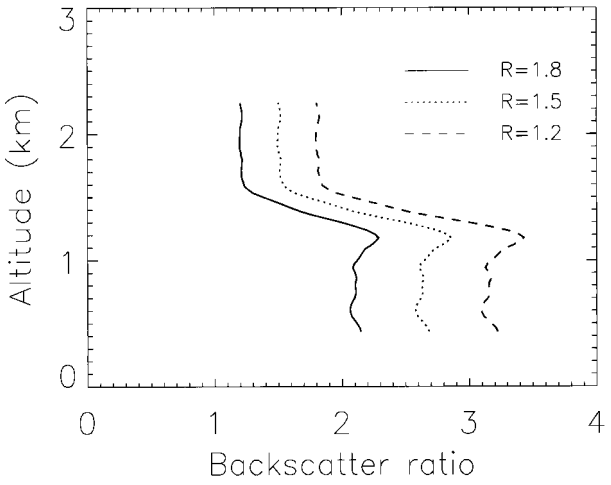

FIG. 3. Scattering ratio profiles obtained close to the shoreline on 11 June 1989 at a wavelength of 760 nm during the 1989 Pressure Experiment. Profiles are given for three values of the scattering ratio boundary condition applied to the lidar signal profile at 2000 m: 1.2, 1.5, and 1.8, for the solid, dotted, and dashed lines, respectively.

which failed to exclude rotational Raman scattering from the lidar signals. We need to account for rotational Raman scattering by oxygen and nitrogen since most of this light will be unabsorbed by oxygen on its way back to the receiver. The total amount of Raman scattering from these two molecules is on the order of 3.5% of the Rayleigh scattering (Korb et al. 1995). We may neglect vibration–rotation Raman scattering as it is another two orders of magnitude smaller than this. Use of a 1-nm bandpass filter would exclude rotational Raman scattering from the measured signals. This would require an offline wavelength closer to the online wavelength.

To account for Raman scattering in the lidar detected online signal, we separate the measured O_2 transmission into its particular and molecular backscatter components including a term to account for the Raman backscatter as

$$\tau(z)_{\text{meas}} = \left\{ \frac{[\beta_p(z) + \beta_m(z)]\tau_{O_2}(z) + 0.035\beta_m(z)T_{O_2}(z)}{\beta_p(z) + \beta_m(z) + 0.035\beta_m(z)} \right\}. \tag{14}$$

In Eq. (14), τ_{O_2} and T_{O_2} are the two- and one-way O_2 transmission, respectively, and 0.035 β_m is the Raman backscatter coefficient. The Raman component of the signal has only the one-way O_2 absorption imposed on the laser light on the outgoing path from the lidar. There is essentially no oxygen resonant extinction for the Raman backscattered signal because of the frequency shift, except for two or three coincidences between O_2 absorption and rotational Raman lines that we assume to be a small fraction of the total Raman signal. Therefore, our error calculations represent a ''worst-case'' error due to Raman contamination. The fraction of the online signal due to Raman scattering will decrease as the aerosol scattering component increases, so that this effect will

[1] The SOFIA (Surface Océanique et Flux à l'Interface Atmosphérique) campaign took place over the Azores in June of 1992 as part of the Atlantic Stratocumulus Experiment. The SEMAPHORE (Structure des Échanges Mer-Atmosphère, Propriétés des Hétérogénéité Océanique Recherche Expérimentale) campaign took place in the same region in October of 1993.

[2] The PYREX (Pyrénées Experiment) campaign was deployed in the Pyrénées region at the French–Spanish border in October and November of 1990.

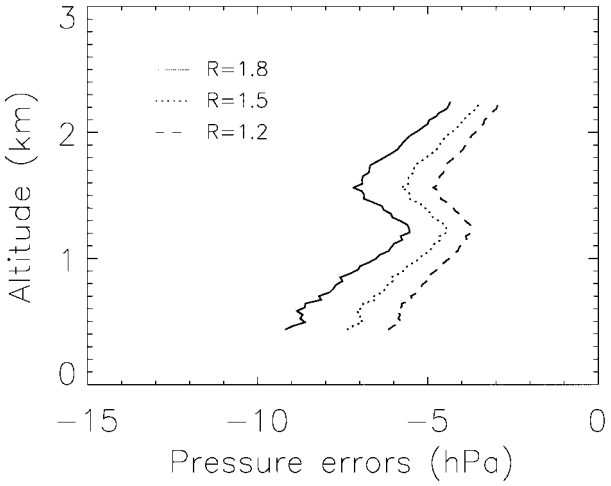

FIG. 4. Pressure error when neglecting the effect of rotational Raman scattering.

be important in relatively aerosol-free atmospheres. We can evaluate the extent of this effect on the measured O_2 transmission by using the scattering ratio estimated from the offline signals.

If $\partial\tau/\tau$ is the fractional difference in the measured transmission and the desired (non-Raman contaminated) transmission, it follows from Eq. (14) that

$$\frac{\partial\tau(z)}{\tau(z)} = \frac{\tau_{\text{meas}}(z) - \tau_{O_2}(z)}{\tau O_2(z)},$$

$$= \left[\frac{R(z) + 0.035/T_{O_2}(z)}{R(z) + 0.035}\right] - 1. \quad (15)$$

Differentiating Eq. (7) with the two-way transmission, we get

$$\partial p(z) = -\frac{1}{4Cp(z)}\frac{\partial\tau(z)}{\tau(z)}. \quad (16)$$

Combining Eqs. (15) and (16),

$$\partial p(z) = -\frac{1}{4Cp(z)}\left\{\left[\frac{R(z) + 0.035/T_{O_2}(z)}{R(z) + 0.035}\right] - 1\right\}. \quad (17)$$

Figure 4 shows the error in the retrieved pressure field from neglecting the effect of the rotational Raman scattering. This was calculated from Eq. (17) using the data from Figs. 1 and 3. The magnitude of the error increases with range in the free troposphere since absorption is increasing with decreasing altitude and a larger fraction of the measured total signal is contributed by Raman scattering. The error temporarily drops as the beam penetrates the mixed layer due to the sudden increase in aerosol backscatter, then continues to increase with absorption as the beam propagates lower into the boundary layer. The Raman signal component causes a maximum error of about −10 hPa near the surface. The constant slope of this error will be, in large part, removed by the calibration procedure described in section 3, leaving the residual error caused by aerosol gradients. In Fig. 4, note that when the signal goes from relatively clear air into a region of high aerosol content, a jump in pressure will be observed in the retrieval (between 1600 and 1300 m).

b. Elastic scattering spectral considerations

The two main scattering phenomena in the atmosphere are Mie scattering for aerosols and Rayleigh scattering for molecules. For Rayleigh scattering, the laser line shape will be broadened by the Brownian motion of the molecular scatterers. Aerosol scattering is affected by Doppler broadening, but its effect is negligible due to the great mass of the aerosols. The DIAL technique for pressure measurements uses the existence of an absorption trough, the region of minimum absorption between two closely spaced strongly absorbing oxygen lines. The trough is formed by the wings of the nearest collision broadened lines where the absorption is pressure sensitive. The lines are selected so that the resultant measurement will be temperature insensitive. The online frequency was taken in the trough region between 13 150 cm^{-1} and 13 154 cm^{-1}, and the offline frequency in a nearby location with minimal resonant absorption but nearly identical attenuation due to scattering and continuum absorption. For the offline detected optical power, we use a simplified form of the lidar equation that uses spectrally integrated quantities:

$$P_{\text{off}}(z) = \frac{T_0 A\eta}{(z_{\text{ref}} - z)^2} E_{\text{off}} \frac{c}{2} (T_{c,\text{off}}(z))^2 [\beta_{p,\text{off}}(z) + \beta_{m,\text{off}}(z)]; \quad (18a)$$

for the online detected power, we write

$$P_{\text{on}}(z) = \frac{T_0 A\eta}{(z_{\text{ref}} - z)^2} E_{\text{on}} \frac{c}{2} [T_{c,\text{on}}(z)]^2 \times [\beta_{p,\text{on}}(z) T_{p,\text{on}}(z) T_{L,\text{on}}(z) + \beta_{m,\text{on}}(z) T_{m,\text{on}}(z) T_{L,\text{on}}(z)], \quad (18b)$$

where $T_{c,\nu}$ is the one-way transmission due to scattering and continuum absorption effects, $T_{L,\nu}$ is the one-way transmission of the laser initial line shape due to resonant absorption effects, and $T_{p,\nu}$ is the resonant one-way transmission on the return path for the Mie scattering. Here, $T_{p,\nu}$ and $T_{L,\nu}$ are nearly identical since the signal is elastically scattered by aerosols, with no change in the shape of the initial laser spectrum other than the modification it undergoes as a result of the spectral structure of the absorption trough. Also, $T_{m,\nu}$ is the resonant one-way transmission experienced by the Doppler broadened Rayleigh backscatter on the return path. Even though the O_2 trough is significantly broader (1.5 cm^{-1}) than the initial laser line (0.015 cm^{-1} full width at half maximum [FWHM]) and the double Doppler broadened backscattered line shape (≈0.06 cm^{-1}

FWHM), the fact that it is not flat will affect the measurements: the larger the line width, the larger the integrated absorption associated with the line shape on the return path. Using Eqs. (18a) and (18b) in Eq. (3), and implementing the usual DIAL assumption that the continuum backscatter coefficient and transmission are equal at the two closely spaced online and offline wavelengths ($\beta_{m,\text{off}} = \beta_{m,\text{on}} = \beta_m$ and $\beta_{p,\text{off}} = \beta_{p,\text{on}} = \beta_p$), the overall two-way transmission between the reference altitude and altitude z can be expressed as

$$\tau_{\text{meas}}(z) = \left[\frac{T_{c,\text{on}}(z)}{T_{c,\text{off}}(z)}\right]^2 \frac{\beta_{p,\text{on}}(z)T_{p,\text{on}}(z)T_{L,\text{on}}(z) + \beta_{m,\text{on}}(z)T_{m,\text{on}}(z)T_{L,\text{on}}(z)}{\beta_{p,\text{off}}(z) + \beta_{m,\text{off}}(z)}$$
$$= \frac{T_{L,\text{on}}(z)}{R(z)}([R(z) - 1]T_{p,\text{on}}(z) + T_{m,\text{on}}(z)). \quad (19)$$

If $\partial\tau/\tau$ is the fractional difference in the measured transmission in the presence of aerosols and the transmission in an aerosol-free atmosphere (τ_m, with $R = 1$), then

$$\frac{\partial\tau(z)}{\tau(z)} = \frac{\tau_{\text{meas}}(z) - \tau_m(z)}{\tau_m(z)}$$
$$= \left[\frac{T_{p,\text{on}}(z)}{T_{m,\text{on}}(z)} - 1\right]\left[1 - \frac{1}{R(z)}\right]. \quad (20)$$

We combine Eqs. (16) and (20) to get the error induced in the pressure retrieval

$$\partial p(z) = -\frac{1}{4Cp(z)}\left[\frac{T_{p,\text{on}}(z)}{T_{m,\text{on}}(z)} - 1\right]\left[1 - \frac{1}{R(z)}\right]. \quad (21)$$

The pressure errors due to the presence of aerosols are shown in Fig. 5 using the aerosol scattering ratio profiles from Fig. 3.

c. Aerosol extinction and backscatter coefficients wavelength dependence

The transmission expressed in Eq. (5) assumes the attenuation due to scattering and continuum absorption to be nearly identical for the online and offline wavelengths. We now drop that assumption to investigate the impact of the wavelength dependence of the extinction and backscatter coefficients (between the online and the offline wavelengths) on the pressure measurements. We still consider these coefficients to have minimal change over the small spectral intervals covered by the backscatter line shapes, however. From Eqs. (18a) and (18b), Eq. (3) can be rewritten as

$$\tau(z)_{\text{meas}} = \left[\frac{T_{c,\text{on}}(z)}{T_{c,\text{off}}(z)}\right]^2 \frac{\beta_{p,\text{on}}(z)T_{p,\text{on}}(z)T_{L,\text{on}}(z) + \beta_{m,\text{on}}(z)T_{m,\text{on}}(z)T_{L,\text{on}}(z)}{\beta_{p,\text{off}}(z) + \beta_{m,\text{off}}(z)},$$
$$= \left(\frac{T_{c,\text{on}}(z)}{T_{c,\text{off}}(z)}\right)^2 \frac{\beta_{p,\text{on}}(z) + \beta_{m,\text{on}}(z)}{\beta_{p,\text{off}}(z) + \beta_{m,\text{off}}(z)}\tau(z). \quad (22)$$

The first part of the right-hand side can be considered as a correction to the transmission as calculated assuming the aerosol extinction and backscatter coefficients to be insensitive to wavelength [i.e., the τ of Eq. (5)]. If $\partial\tau/\tau$ is the fractional difference in the measured transmission and the desired transmission, Eq. (22) can be used:

$$\frac{\partial\tau(z)}{\tau(z)} = \frac{\tau(z)_{\text{meas}} - \tau(z)}{\tau(z)}$$
$$= \left[\frac{T_{c,\text{on}}(z)}{T_{c,\text{off}}(z)}\right]^2 \frac{\beta_{p,\text{on}}(z) + \beta_{m,\text{on}}(z)}{\beta_{p,\text{off}}(z) + \beta_{m,\text{off}}(z)} - 1. \quad (23)$$

To get the error induced in the pressure retrieval, we combine Eqs. (16) and (23):

$$\partial p(z) = -\frac{1}{4Cp(z)}\left\{\left[\frac{T_{c,\text{on}}(z)}{T_{c,\text{off}}(z)}\right]^2 \frac{\beta_{p,\text{on}}(z) + \beta_{m,\text{on}}(z)}{\beta_{p,\text{off}}(z) + \beta_{m,\text{off}}(z)} - 1\right\}. \quad (24)$$

The impact of the aerosol wavelength dependence for DIAL measurements made over the Atlantic was tested using the maritime aerosol model described by Flamant et al. (1998). Based on the works of Shettle and Fenn (1979) and Gathman (1983), the model assumes a log-normal size distribution for the mixture of sulphate and

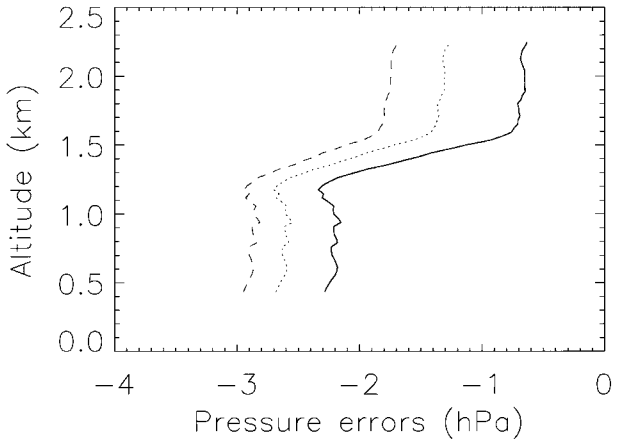

FIG. 5. Pressure errors due to the presence of aerosols corresponding to the aerosol scattering ratio profiles of Fig. 3.

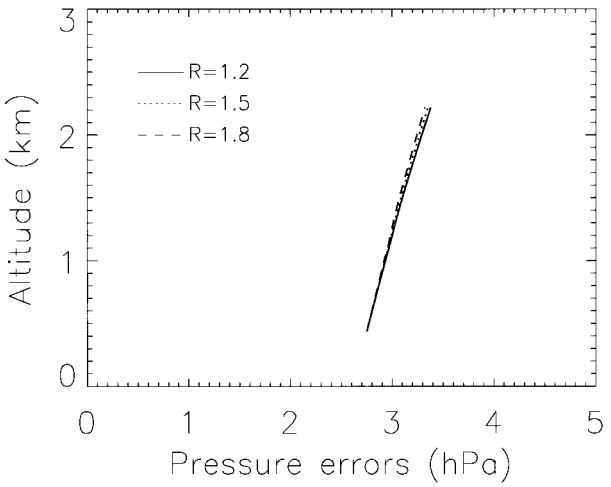

FIG. 6. Pressure error when neglecting the effect of aerosol backscatter and extinction coefficients wavelength dependence for the aerosol scattering ratios of Fig. 3.

sea-salt aerosols in the lower troposphere. Since lidar signal intensity is very sensitive to relative humidity (Dupont et al. 1994), the aerosol refractive index dependence on relative humidity is also introduced and modeled according to relationships previously proposed by Hänel (1972). Typical values for sulphate concentration off the eastern shore are taken from Hoppel et al. (1990). We have selected a concentration of 2000 particles cm^{-3} as representative of the polluted air masses flowing off shore. The concentration of sea salt increases with surface wind speed (Blanchard and Woodcock 1980), and a background value of 5 particles cm^{-3} is chosen. It is representative of the sea-salt burden in the marine atmospheric boundary layer resulting from the action of wind on the surface for a period of at least 12 h. This rate is assumed constant in the PBL for a given wind speed. Aloft, in order to account for the decreasing sea-salt aerosol concentration, a 2-km scale height is introduced.

A Mie model is used to calculate the backscatter and extinction coefficients for the sulfate and sea-salt aerosols at 757 and 760 nm. The maritime particulate mixture phase function profile is then deduced from a relative humidity profile and the fractional concentration of sea-salt dependence with height. The sulfate and sea-salt aerosol extinction and backscatter coefficients wavelength dependence are calculated according to

$$\delta_\alpha = \frac{\ln[\alpha(\lambda_2)/\alpha(\lambda_1)]}{\ln(\lambda_2/\lambda_1)} \quad \text{for } \lambda_2 \geq \lambda_1 \qquad (25a)$$

and

$$\delta_\beta = \frac{\ln[\beta(\lambda_2)/\beta(\lambda_1)]}{\ln(\lambda_2/\lambda_1)} \quad \text{for } \lambda_2 \geq \lambda_1, \qquad (25b)$$

where $\lambda_2 = 760$ nm and $\lambda_1 = 757$ nm. The Ångström coefficients δ_α and δ_β calculated from Eqs. (25a) and (25b) will be used to estimate the difference in transmission between the online and offline wavelength given by Eq. (23). However, δ_α and δ_β also depend on relative humidity. Since we expect typical values to be quite different in the free troposphere and in the boundary layer, the humidity profile measured at Wallops was used to calculate these coefficients throughout the lower troposphere. Table 2 summarizes the value of the Ångström coefficients for extinction and backscatter for relative humidities of 5% and 50%, representative of the free troposphere and the boundary layer, respectively.

We show the resulting error for a surface wind speed of 7 m s^{-1} (Fig. 6). The value of the surface wind speed does not introduce any additional bias. The extinction and backscatter wavelength dependence induces a systematic bias on pressure retrievals. However, errors are not significantly different in the free troposphere and in

TABLE 2. Typical wavelength dependence of the extinction and backscatter coefficients between 757 and 760 nm for the sea-salt and sulfate aerosols, as well as sea-salt/sulphate aerosols mixture.

	Ångström coefficient					
	Extinction (δ_α)			Backscatter (δ_β)		
	Sea salt	Sulfate	Mixture	Sea salt	Sulfate	Mixture
Free troposphere	0.15	−1.4	−1.3	−0.4	−2.1	−1.8
Boundary layer	0.10	−2.1	−0.8	−1.6	−1.6	−1.6

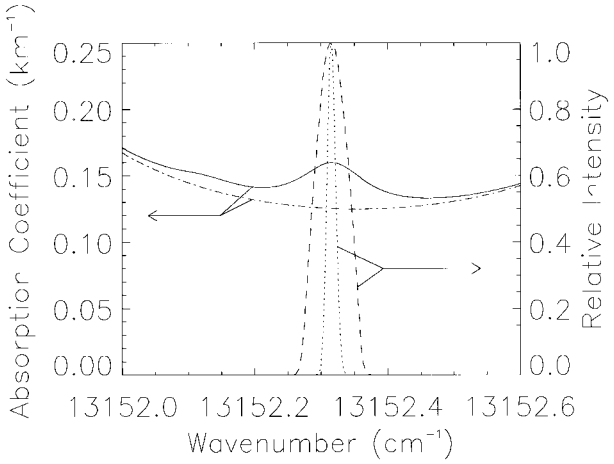

FIG. 7. Calculated absorption spectrum for O_2 in the region of the DIAL measurements with (solid line) and without (dashed–dotted line) the isotopic lines. Superimposed is the laser output spectrum (dotted line) and Rayleigh broadened backscatter (dashed line) relative to the O_2 absorption spectrum.

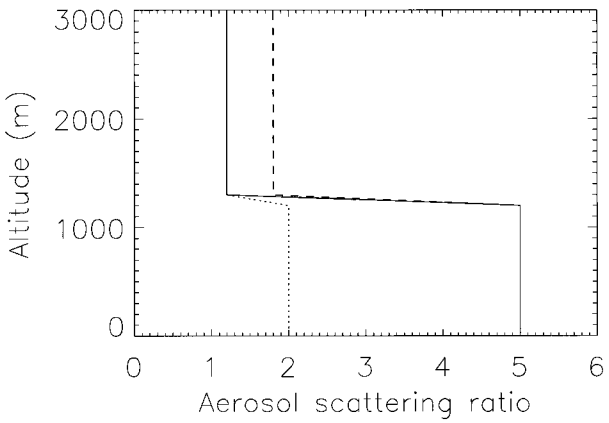

FIG. 8. Backscatter ratio models used to calculate the effect of Rayleigh broadening in isotopic line effects. Two models use $R = 1.2$ in the free troposphere with $R = 5$ (solid line) and $R = 2$ (dashed line) in the PBL. The third model (dotted line) uses $R = 1.8$ in the free troposhere and $R = 5$ in the PBL.

the PBL. This is caused by the relatively close values of δ_α (and δ_β) in these two regions (see the Ångström coefficients for the sea-salt and sulphate aerosol mixture in Table 2).

d. Isotopic oxygen lines

Isotopic lines have been observed in the O_2 spectrum in long-path atmospheric spectroscopic measurements by Babcock and Herzberg (1948). From their measurements one expects to observe an O^{16}–O^{18} line in the center of the trough we used for pressure measurements. Figure 7 shows a calculated absorption spectrum near the 1000-hPa level assuming a line strength equal to the strength of the same transition in O^{16}–O^{16}. We attempted to locate this line with the lidar in flight by tuning the laser across the absorption trough while observing a real-time display of atmospheric transmission integrated over a portion of the path below the aircraft. We failed to observe the isotopic line due to inadequate signal to noise over reasonable integration times of a few seconds. Alternatively, we located the laser frequency where we thought it should be to avoid the isotopic line by interpolating between the sides of the O^{16}–O^{16} lines as measured on the real-time display. However, this technique may also be of questionable accuracy for the same reason we failed to observe the isotopic line. Therefore, we studied what would happen if the laser were actually located on the isotopic line.

To help visualize the spectral processes, refer to Fig. 7, where we have plotted the O_2 spectrum in the boundary layer with and without the isotopic line, the laser output spectrum, and the Rayleigh broadened component of the laser backscatter. The isotopic line adds about 30% to the trough absorption at the line center. We note that the collision broadened line profile central absorption is altitude independent since the decrease in absorption due to a redistribution of the molecular population into the wings of the profile due to increasing pressure is exactly offset by the increase in density (Korb and Weng 1982). Therefore, this additional absorption, to first order, is pressure independent in the center, gradually changing over to a p^2 dependence as the frequency moves farther from the line center. The laser spectrum was measured by Korb et al. (1995) to consist of three nearly equally spaced modes separated by 0.007 cm^{-1}, the two outer modes being half as intense as the central mode. The laser spectrum envelope can be approximated by a Gaussian profile with a half width equal to the mode spacing.

For a description of the mathematical representation of the lidar formulation, which includes the frequency dependence of the laser light and Rayleigh scattering, we refer the reader to Ansmann and Bosenberg (1987).

For the purposes of modeling the effect of the isotopic line absorption on the Rayleigh broadened and aerosol backscatter, we use three modeled atmospheres having backscatter profiles similar to our data, as represented in Fig. 8. We calculated lidar signals using our system parameters with the online signals as a function of frequency. Figure 9 represents the online return signal spectra at four altitude levels in an atmosphere characterized by a backscatter ratio of 5 in the PBL and 1.2 in the free troposphere. The outgoing laser energy is concentrated within the isotopic absorption line and experiences a stronger absorption coefficient. The backscattered energy is distributed into the wings of the isotopic line and experiences a smaller spectrally integrated absorption coefficient. With the laser centered on the isotopic line, the immediate effect of the aerosols is to force more of the backscatter into the isotopic absorption line, therefore increasing the net absorption. As the laser beam propagates down through the atmosphere,

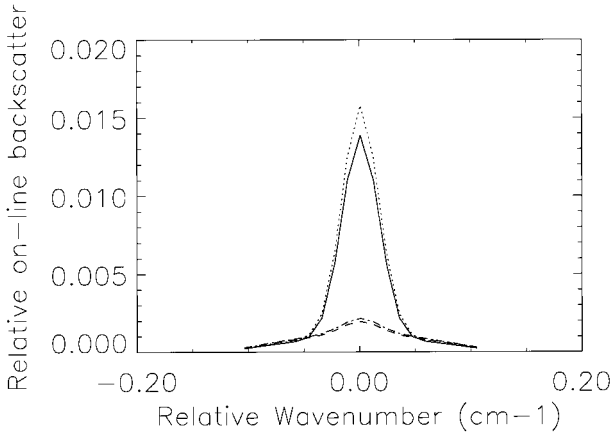

FIG. 9. The online return signal spectra at various altitude levels, 100 (solid line), 800 (short-dashed line), 1500 (long-dashed line), and 2200 m (short and long-dashed line) in an atmosphere characterized by a backscatter ratio of 5 in the boundary layer and 1.8 above.

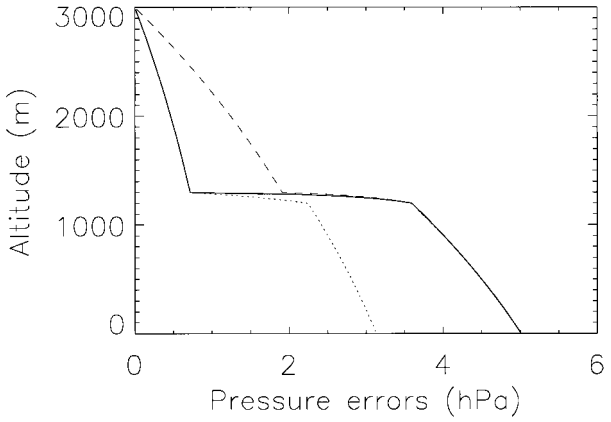

FIG. 10. Errors in the retrieved pressure profile due to isotopic line interference. The line styles correspond to those representing their respective scattering models in Fig. 8.

its spectral shape changes, broadening if centered on the isotopic line, or if off-center, becoming asymmetric. This effect is minor compared to the variation in aerosol scattering, however. The net 30% offset in the absorption baseline due to the presence of the isotopic line is not a source of error since it acts as a net change to the O^{16}–O^{16} line strength, which is accounted for in the calibration procedure discussed in the section on instrumental errors.

To evaluate the error in the retrieved pressure profiles caused by ignoring the effect of Rayleigh broadening in the presence of the isotopic line, we analyze the oxygen transmission calculated for combined aerosol and molecular scattering and compare it to the oxygen transmission calculated for molecular scattering only. We could compare it to aerosol only scattering, which would more closely conform to the often-made lidar assumption of monochromicity, but we chose pure Rayleigh scattering for consistency with our other corrections and the more realistic limit of having zero aerosols as opposed to zero molecules. To quantify this effect we use Eq. (21).

The oxygen transmission for the molecular scattered light and particulate scattered light are calculated using laboratory line parameters measured by Burch and Gryvnak (1969), and line frequencies measured by Babcock and Herzberg (1948), in a Voigt line shape algorithm. Using the modeled lidar backscatter profiles from Fig. 8, we estimate the errors in the pressure profile caused by not accounting for isotopic absorption using Eq. (21), plotting the results in Fig. 10. Because aerosol scattering is concentrated at the line center, the effective absorption coefficient is larger for aerosol backscatter than for molecular backscatter. Hence, the model with greater aerosol scattering in the free troposphere shows larger pressure errors. The increased aerosol backscatter from the PBL causes even higher errors. From this figure, one can see that any aerosol structure will create a correlated false structure in the retrieved pressure field. But what happens when the laser frequency is somewhere else in relation to the isotopic line? This is illustrated in Fig. 11, where we have plotted the errors for the worst-case model from Fig. 10, and having the laser located at one, two, and three half-widths from the isotopic line center, as well as on line center. At one half-width, the laser is centered on a linear region on the side of the line profile. Refer back to Fig. 7 to help visualize this. If one spectrally integrates over the molecular backscatter line shape, the effective absorption coefficient is about the same as that for the aerosol line shape since energy on the higher absorbing side of the laser center frequency is compensated for by lower absorption on the opposite side. This is why the errors are close to zero at all altitudes. When the laser is located at two half-widths from the isotopic line center, the molecular backscatter contains a larger portion of energy in the isotopic line

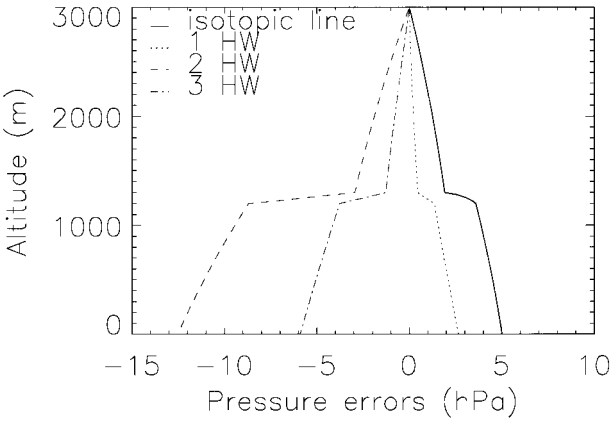

FIG. 11. Pressure errors for the worst-case aerosol model ($R = 1.8$ in free troposphere and $R = 5$ in PBL) due to the laser being on the isotopic line and the errors for the laser being one, two, and three half-widths off the isotopic line.

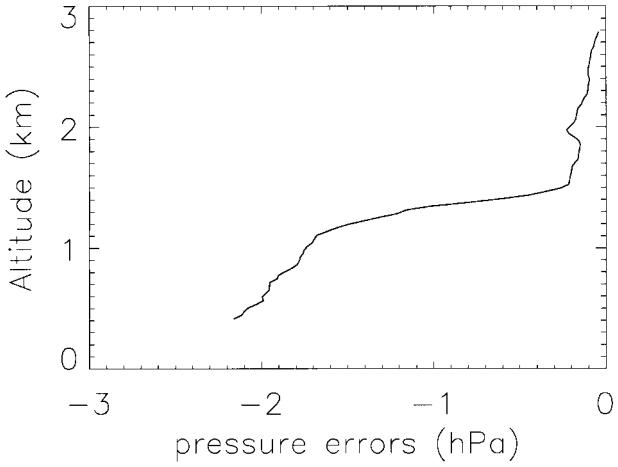

FIG. 12. Pressure errors caused by the presence of water vapor in the atmosphere near the beginning of track A. Water vapor decreases the oxygen mixing ratio and thereby increases the transmission.

than does the aerosol backscatter. Hence, the spectrally integrated absorption coefficient is larger for molecular than for aerosol backscatter, and the errors are negative instead of positive. As the laser is located even farther from the line center, the errors will decrease in magnitude, as does the curve for the three half-widths away in Fig. 11.

e. Water vapor effects

Water vapor affects the pressure measurements by lowering the mixing ratio of oxygen. For an integrated path measurement, that is, the two-way transmission, this effect is partially compensated due to the lower average mass of air particles. The pressure measurement error for relative humidity values of 20%–80% amounts to 0.05% for altitudes above 2 km and 0.1% for measurements extending to ground level (Korb et al. 1995). This error could amount to as much as 1 hPa at 1000 hPa and since we are trying to correct for errors of this magnitude, the water vapor effect needs to be considered. Using radiosonde humidity data and a transmission profile, the pressure errors can be estimated using Eq. (16). The fractional change in the transmission can be estimated as

$$\frac{\partial\tau(z)}{\tau(z)} = \frac{\tau_{wv}(z) - \tau_{O_2}(z)}{\tau_{O_2}(z)},$$

$$= \exp[2w' t_{O_2}(z)] - 1, \qquad (26)$$

where τ_{wv} is the two way transmission for the decreased oxygen mixing ratio. The integrated optical depth for dry air, t_{O_2}, and the integrated optical depth for moist air, t_{wv}, can can be related by $t_{wv} = (1 - w')t_{O_2}$, with w' the fractional volume of water vapor. For a reasonable estimate of the optical depth, we used the first transmission profile from flight leg A to get the two-way integrated optical depths using Eq. (5). The water vapor mixing ratio is calculated from the radiosonde data and converted to a fractional volume by correcting for the average mass of an atmospheric molecule, $w' = w \times 29.23/18.016$, where w is the water vapor mass mixing ratio. The constant C in Eq. (16) also needs a mass correction for the decrease in the average mass of the molecule. Figure 12 shows a plot of these errors versus altitude for a profile near the beginning of track A. Above the boundary layer, the errors are less than 0.25 hPa, and in the boundary layer the errors are approximately 2 hPa. Figure 12 shows the importance of correcting for the water vapor content of the atmosphere, at least in the boundary layer.

6. Summary and conclusions

We have analyzed the sensitivity of differential absorption lidar measurements of the atmospheric pressure profile to instrumental and atmospheric systematic error sources. The errors are evaluated for airborne lidar measurements made off the mid-Atlantic coast of the United States in 1989, as if they were uncorrected for. They are summarized in Table 3. Large errors can result by ignoring the effects of Raman scattering, strong aerosol gradients, wavelength dependence of the aerosol backscatter coefficient, Doppler broadening in the presence of an isotopic oxygen line, and water vapor vertical distribution. All of these errors are strongly correlated with structure in the aerosol backscatter profiles and systematically add. They can introduce large pressure gradients on the horizontal since the lidar signal is highly sensitive to aerosol content and relative humidity, which in turn relate, at small scales, to convective ac-

TABLE 3. Systematic error on pressure retrievals caused by instrumental and atmospheric effects (in hPa) considered individually.

	Atmospheric effects					Instrumental effects
	Rotational Raman	Doppler broadening	Wavelength dependence	Isotopic lines	Water vapor	Baseline subtraction
Free troposphere						
$R = 1.2$	−7.0 to −4.0	−1.0	3.0–3.6	−1.5 to 0.8	−0.2 to 0	−0.15 to 0.15
$R = 1.8$	−4.0 to −2.0	−2.0	2.8–3.3	−4.0 to 2.0	−0.2 to 0	−0.15 to 0.15
Boundary layer						
$R = 2$	−12.0 to −6.0	−2.2	2.7–3.0	−7.2 to 3.0	−2.0 to −0.2	−0.3 to 0.3
$R = 5$	−6.0 to −3.0	−5.0	2.7–2.8	−12.0 to 5.0	−2.0 to −0.2	−0.3 to 0.3

tivity in the PBL, and, at larger scales, to stratification and coastal influence in terms of aerosol population.

A correction scheme is derived for each effect and will be applied to pressure profile retrievals from the 1989 flight experiments in a companion paper, Part II, and the accuracy to which the retrievals are made will be evaluated.

Acknowledgments. Support for this work was provided by Dr. John Theon and Dr. Ramesh Kakar of NASA headquarters; direction of Cyrille Flamant's grant by Prof. Thomas D. Wilkerson; technical support by Dr. Coorg Prasad (presently with Science and Engineering Services, Inc., Burtonsville, Maryland) and Mr. Joseph Famiglietti, NASA/GSFC. The authors would like to thank Dr. Patrick Chazette of CEA and Drs. Jacques Pelon, Pierre H. Flamant, and Vincent Trouillet of CNRS for many helpful discussions.

REFERENCES

Ansmann, A., 1985: Errors in ground-based water-vapor DIAL measurements due to Doppler-broadened Rayleigh backscatter. *Appl. Opt.,* **24,** 3476–3480.

——, and J. Bosenberg, 1987: Correction scheme for spectral broadening by Rayleigh scattering in differential absorption lidar measurements of water vapor in the troposphere. *Appl. Opt.,* **26,** 3026–3032.

Babcock, H. D., and L. Herzberg, 1948: Fine structure of the red system of atmospheric oxygen bands. *Astrophys. J.,* **108,** 167–190.

Blanchard, C. D., and A. H. Woodcock, 1980: The production, concentration, and vertical distribution of the sea-salt aerosol. *Ann. N. Y. Acad. Sci.,* **338,** 330–347.

Bond, N. A., and R. G. Feagle, 1985: Structure of a cold front over the ocean. *Quart. J. Roy. Meteor. Soc.,* **111,** 739–759.

Brown, R. A., and G. Levy, 1986: Ocean surface pressure fields from satellite-sensed winds. *Mon. Wea. Rev.,* **114,** 2197–2206.

Bufton, J. L., F. E. Hodge, and R. N. Swift, 1983: Airborne measurements of laser backscatter from the ocean surface. *Appl. Opt.,* **22,** 2603–2618.

Burch, D. E., and D. A. Gryvnak, 1969: Strengths, widths, and shapes of the oxygen lines near 13,100 cm^{-1} (7620 A). *Appl. Opt.,* **8,** 1493–1499.

Cox, C., and W. Munk, 1954: Measurements of roughness of the sea surface from photographs of the sun's glitter. *J. Opt. Soc. Amer.,* **44,** 838–850.

Dupont, E., J. Pelon, and C. Flamant, 1994: Study of the moist convective boundary layer structure by backscatter lidar. *Bound.-Layer Meteor.,* **69,** 1–25.

Flamant, C., and J. Pelon, 1996: Atmospheric boundary-layer structure over the Mediterranean during a Tramontane event. *Quart. J. Roy. Meteor. Soc.,* **122,** 1741–1778.

——, V. Trouillet, P. Chazette, and J. Pelon, 1998: Wind speed dependence of the atmospheric boundary layer optical properties and ocean surface reflectance as observed by airborne backscatter lidar. *J. Geophys. Res.,* **103** (C11), 25 137–25 158.

Gathman, S. G., 1983: Optical properties of the marine aerosols as predicted by the Navy aerosol model. *Opt. Eng.,* **22,** 57–62.

Hänel, G., 1972: Computation of extinction of visible radiation by atmospheric aerosol particles as a function of the relative humidity based upon measured properties. *Aerosol Sci.,* **3,** 377–386.

Hoppel, W. A., J. W. Fitzgerald, G. M. Frick, R. E. Larson, and E. J. Mack, 1990: Aerosol size and optical properties found in the marine boundary layer over the Atlantic Ocean. *J. Geophys. Res.,* **95** (D4), 3659–3686.

Klett, J. D., 1985: Lidar inversion with variable backscatter/extinction ratios. *Appl. Opt.,* **24,** 1638–1643.

Korb, C. L., and C. Y. Weng, 1982: A theoretical study of a two wavelength lidar technique for the measurement of atmospheric temperature profiles. *J. Appl. Meteor.,* **21,** 1346–1355.

——, and ——, 1983: Differential absorption lidar technique for measurement of the atmospheric pressure profile. *Appl. Opt.,* **22,** 3759–3770.

——, G. K. Schwemmer, M. Dombrowski, and C. Y. Weng, 1989: Airborne and ground-based lidar measurements of the atmospheric pressure profile. *Appl. Opt.,* **28,** 3015–3020.

——, ——, J. Famiglietti, H. Walden, and C. Prasad, 1995: Differential absorption lidars for remote sensing of the atmospheric pressure and temperature profiles: Final report. NASA Tech. Memo. 104618, 249 pp. [Available from G. Schwemmer, NASA/Goddard Space Flight Center, Code 912, Greenbelt, MD 20771.]

Lee, H. S., G. K. Schwemmer, C. L. Korb, M. Dombrowski, and C. Prasad, 1989: Gated photomultiplier response characterization for DIAL measurements. *Appl. Opt.,* **29,** 3303–3315.

Nuss, W., and. R. A. Brown, 1987: Evaluation of surface wind and flux analysis techniques using conventional data in marine cyclones. *Dyn. Atmos. Oceans,* **10,** 291–315.

Sasano, Y., and E. V. Browell, 1989: Light scattering characteristics of various aerosol types derived from multiple wavelength lidar observations. *Appl. Opt.,* **28,** 1670–1679.

Schwemmer, G. K., M. Dombrowski, C. L. Korb, J. Milrod, H. Walden, and R. H. Kagann, 1987: A lidar system for measuring atmospheric pressure and temperature profiles. *Rev. Sci. Instrum.,* **58,** 2226–2237.

Shettle, E. P., and R. W. Fenn, 1979: Models for aerosols of the lower atmosphere and the effects of humidity variations on their optical properties. Air Force Geophysics Laboratory Environment Research Paper 678, AFGL-TR-79-0214, 94 pp. [NTIS ADA 085951.]

Starr, D. O., C. L. Korb, G. K. Schwemmer, and C. Y. Weng, 1992: Observations of height-dependent pressure perturbation structure of a strong mesoscale gravity wave. *Mon. Wea. Rev.,* **120,** 2808–2820.

Theopold, F., and J. Bosenberg, 1993: Differential absorption lidar measurements of atmospheric temperature profiles: Theory and experiment. *J. Atmos. Oceanic Technol.,* **10,** 165–179.